1-1-2018

Elaborately assembled core-shell structured metal sulfides as a bifunctional catalyst for highly efficient electrochemical overall water splitting

Yanna Guo
Waseda University

Jing Tang
National Institute For Materials Science, Japan

Zhongli Wang
National Institute for Materials Science, Japan

Yong-Mook Kang
Dongguk University, dake1234@dongguk.edu

Yoshio Bando
University of Wollongong, yoshio@uow.edu.au

See next page for additional authors

Elaborately assembled core-shell structured metal sulfides as a bifunctional catalyst for highly efficient electrochemical overall water splitting

Abstract

Low efficiency, short lifetimes, and limited kinds of catalysts are still three fundamental shortcomings that have plagued electrochemical water splitting. Herein, we rationally synthesized a cost-effective Co 3 S 4 @MoS 2 hetero-structured catalyst that has proven to be a highly active and stable bifunctional catalyst for both hydrogen evolution reaction (HER) and oxygen evolution reaction (OER) in an alkaline environment. The heterostructure was obtained via a first hydrothermal approach to obtain hollow Co 3 S 4 nanoboxes based on the ionic exchange reaction between Fe(CN) 6 3− of Co-Fe Prussian blue analogue (PBA) and S 2− at 120 °C, and the subsequent in situ growth of MoS 2 nanosheets on the surface of Co 3 S 4 nanoboxes at an elevated temperature of 200 °C. The synergistic effects between the active and stable HER catalyst of MoS 2 and the efficient OER catalyst of Co 3 S 4 , as well as the morphological superiority of hollow and core-shell structures, endow Co 3 S 4 @MoS 2 with remarkable electrocatalytic performance and robust durability toward overall water splitting. As a result, the designed non-noble electrocatalyst of Co 3 S 4 @MoS 2 exhibits a low overpotential of 280 mV for OER and 136 mV for HER at a current density of 10 mA cm −2 in an alkaline solution. Meanwhile, a low cell voltage of 1.58 V is achieved by using the heterostructure as both anode and cathode catalysts. This work paves the way to the design and construction of other prominent electrocatalysts for overall water splitting.

Disciplines

Engineering | Physical Sciences and Mathematics

Publication Details

Guo, Y., Tang, J., Wang, Z., Kang, Y., Bando, Y. & Yamauchi, Y. (2018). Elaborately assembled core-shell structured metal sulfides as a bifunctional catalyst for highly efficient electrochemical overall water splitting. Nano Energy, 47 494-502.

Authors

Yanna Guo, Jing Tang, Zhongli Wang, Yong-Mook Kang, Yoshio Bando, and Yusuke Yamauchi

Elaborately Assembled Transition Metal Chalcogels as a Bifunctional Catalyst for Highly Efficient Electrochemical Overall Water Splitting

Yanna Guo,[a,b] Jing Tang,[a]* Zhongli Wang,[a] Yoshio Bando,[a, c] and Yusuke Yamauchi[a,b,c,d]*

[a] International Center for Materials Nanoarchitectonics (MANA), National Institute for Materials Science (NIMS), 1-1 Namiki, Tsukuba, Ibaraki 305-0044, Japan. E-mail: TANG.Jing@nims.go.jp

[b] Faculty of Science and Engineering, Waseda University, 3-4-1 Okubo, Shinjuku, Tokyo 169-8555, Japan

[c] Australian Institute for Innovative Materials (AIIM), University of Wollongong, North Wollongong, NSW 2500, Australia. E-mail: yusuke@uow.edu.au

[d] School of Chemical Engineering and Australian Institute for Bioengineering and Nanotechnology (AIBN), The University of Queensland, Brisbane, QLD 4072, Australia

Abstract

Low efficiency, short lifetimes, and limited kinds of catalysts are still three fundamental shortcomings that have plagued electrochemical water splitting. Herein, we rationally synthesized a cost-effective Co_3S_4@MoS_2 hetero-structured catalyst that has proven to be a highly active and stable bifunctional catalyst for both hydrogen evolution reaction (HER) and oxygen evolution reaction (OER) in an alkaline environment. The heterostructure was obtained *via* a first hydrothermal approach to obtain hollow Co_3S_4 nanoboxes based on the ionic exchange reaction between $Fe(CN)_6^{3-}$ of Co-Fe Prussian blue analogue (PBA) and S^{2-} at 120 ºC, and the subsequent *in-situ* growth of MoS_2 nanosheets on the surface of Co_3S_4 nanoboxes at an elevated temperature of 200 ºC. The synergistic effects between the active and stable HER catalyst of MoS_2 and the efficient OER catalyst of Co_3S_4, as well as the morphological superiority of hollow and core-shell structures, endow Co_3S_4@MoS_2 with remarkable electrocatalytic performance and robust durability toward overall water splitting. As a result, the designed non-noble electrocatalyst of Co_3S_4@MoS_2 exhibits a low overpotential of 280 mV for OER and 136 mV for HER at a current density of 10 $mA \cdot cm^{-2}$ in an alkaline solution. Meanwhile, a low cell voltage of 1.58 V is achieved by using the heterostructure as both anode and cathode catalysts. This work paves the way to the design and construction of other prominent electrocatalysts for overall water splitting.

Keywords: core-shell; hollow cube; metal chalcogel heterostructure; bifunctional catalyst; water splitting

1. Introduction

Today, the demand for renewable energy is increasing due to the looming energy and environmental problems generated by the combustion of traditional energy resources (*e.g.*, coal, oil and natural gas) [1-3]. To achieve sustainable energy production, it is urgent to develop advanced energy conversion techniques for lessening the burden of energy demand. Electrochemical water splitting is acknowledged as a powerful technology that benefits from its high-purity H_2 production with zero environmental emissions [4,5]. The hydrogen evolution reaction (HER) and the oxygen evolution reaction (OER) are the two half reactions of water splitting. Currently, noble metal-based materials, such as Pt- and Ir/Ru-based materials, are still the most efficient catalysts for HER and OER with low overpotentials and fast kinetics [6,7]. However, the high cost and scarcity of these noble metals severely impede their large-scale application. Therefore, research into and development of alternative electrocatalysts based on earth-abundant materials has attracted considerable interest [8-10]. Heretofore, a broad range of earth-abundant electrocatalysts have been developed for either HER (*e.g.*, molybdenum-based sulfides [11,12], carbides [13,14], and phosphides [15]) or OER (*e.g.*, transition metal-based oxides [16,17], layered double hydroxides [18,19], and sulfides [20,21]); some of them even performed comparably to noble metals. However, it is still difficult to pair HER and OER electrode reactions together in an integrated electrolyzer due to the mismatch of pH ranges in which these catalysts remain stable and highly active. For instance, molybdenum disulfide (MoS_2) has been extensively investigated as a stable electrocatalyst for HER in a wide pH range from acid to alkaline (especially in acid electrolyte) due to its high chemisorption capability for hydrogen, but it has a poor catalytic performance for OER. Cobalt sulfides have been making strides as efficient electrocatalysts for OER, whereas they are not stable in acid electrolytes. Thus, taking the convenience and cost reduction into account, the development of a versatile catalyst with high activity toward both the HER and OER in the same electrolyte is technologically important yet challenging.

One effective way of realizing a bifunctional electrocatalyst with high activity

for both the HER and OER is to tune the compositions of catalysts through doping heteroatoms or integrating different components. Generally, hybrid catalysts would exhibit an enhanced electrocatalytic activity due to increased conductivity and more exposed active sites deriving from the synergistic effects between the different components. For example, Staszak-Jirkovský and co-workers [22] designed a CoS_x/MoS_x hybrid catalyst for the efficient electrocatalytic production of hydrogen in both alkaline and acidic environments. After building an electrochemically interfacial model and studying the structure-activity-stability relationships between CoS_x and MoS_x, they proposed that the high activity and stability of the obtained CoS_x/MoS_x catalyst is governed by a synergy between the electronic effects (substrate–adsorbate binding energies) and morphological effects (number of defects). Zhang and co-workers [23] assembled a high-activity MoS_2/Ni_3S_2 electrocatalyst for overall water splitting through interface engineering. In combination with density functional theory (DFT) calculations, they demonstrated that the constructed interfaces between MoS_2 and Ni_3S_2 synergistically favor the chemisorption of hydrogen and oxygen-containing intermediates, thus accelerating overall electrochemical water splitting. Feng and co-workers [24] developed a hierarchical cobalt sulfide/nickel selenide aligned on an exfoliated graphene hybrid electrocatalyst as an efficient electrode for splitting water. The enhanced activity of the obtained material is driven by strong electron-electron interactions and interface reconstruction between Ni_3Se_2 and Co_9S_8 through Ni-S bonding.

Furthermore, elaborately combining synergistic components into a well-designed architecture is also an effective way to improve the electrochemical performance of catalysts. Metal-organic frameworks (MOFs) [25,26], formed by the metal ions and organic ligands via strong coordination bonds, have been widely used as precursors for the fabrication of various functional materials, including carbon, metal-containing compounds and composites [27]. More importantly, MOFs can work as templates to guide the resultant morphology and structure. To date, different morphologies, such as hollow polyhedra [28], nanoframes [29], and multilayer core-shells [30], have been successfully synthesized by using MOFs as templates. Specially, MOF-derived

hollow structures draw a lot of attention due to their abundant active sites, fast mass transfer and short electrolyte diffusion pathway.

Bearing these points in mind, we designed a highly efficient overall water splitting catalyst by integrating the OER active Co_3S_4 building blocks with the stable HER catalyst of MoS_2 units into a compact and robust three-dimensional (3D) Co_3S_4@MoS_2 heterostructure. Co-Fe Prussian blue analogue (PBA) was selected as both a morphological template and a precursor, and then a hollow cubic Co_3S_4@MoS_2 heterostructure was obtained by using a two-step temperature-raising hydrothermal reaction process. This unique 3D hollow heterostructure of Co_3S_4@MoS_2 integrates the advantages of two different phases and builds strong interfacial coupling between the inner Co_3S_4 core and outer MoS_2 shell, which all favor its bifunctional electrochemical activity for the OER and HER in alkaline media. Furthermore, Co_3S_4@MoS_2 has proven to be a low-cost alternative electrocatalyst for overall water splitting in an alkaline environment when assembled into a two-electrode setup.

2. Experimental section

Chemicals

Cobalt nitrate hexahydrate ($Co(NO_3)_2 \cdot 6H_2O$), sodium citrate dehydrate, potassium hexacyanoferrate(Ⅲ), thioacetamide (CH_3CSNH_2), and sodium sulfide nonahydrate ($Na_2S \cdot 9H_2O$) were purchased from Wako Co. Nafion solution (5 wt %) and sodium molybdate dihydrate ($Na_2MoO_4 \cdot 2H_2O$, 99.5%) were purchased from Sigma-Aldrich Corp. All chemicals were used without further purification.

Material preparation

Synthesis of a Co-Fe Prussian blue analogue (PBA) template

The typical reaction condition for the preparation of a Co-Fe PBA template is as follows: cobalt nitrate hexahydrate (1.5 mmol) and sodium citrate dihydrate (2.25 mmol) were dissolved in 50 mL deionized (DI) water to form a clean solution. Then, a 50 mL solution containing 1 mmol potassium hexacyanoferrate(Ⅲ) was poured into the solution and shaken vigorously for 3 min. The solution mixture was aged for another 24 h at room temperature. After that, the precipitates were collected by centrifugation, washed with water several times, and dried at 60 °C overnight.

Synthesis of a hollow Co_3S_4@MoS_2 heterostructure

Fifty mg of the resultant Co-Fe PBA was dispersed in 12 mL of ethanol under ultrasonication for half an hour to obtain a uniform solution. Then, 6 mL of Na_2S solution (10 mg/mL) was dropped into the above suspension under magnetic stirring for a few minutes, followed by the addition of 4 mL of thioacetamide (0.1875 mM, ethanol) and 4 mL of $Na_2MoO_4 \cdot 2H_2O$ (0.0625 mM, water) under stirring for 10 min for each solution. Afterward, the mixture was transferred to a Teflon-lined stainless steel autoclave (50 mL) and kept at 120 °C for 6 h; the temperature was then increased to 200 °C and kept for another 12 h. After cooling to room temperature, the obtained black products were washed with DI water and ethanol several times and then dried at 60 °C overnight. Finally, they were annealed at 350 °C for 2 h under a N_2 atmosphere to obtain a highly crystalline Co_3S_4@MoS_2 heterostructure. The heating rate was 1 °C·min^{-1}.

Furthermore, pure Co_3S_4 and MoS_2 were also prepared for comparison and to highlight the structural advantages of the Co_3S_4@MoS_2 heterostructure. Co_3S_4 nanoboxes were synthesized as follows: 6 mL of Na_2S (10 mg/mL) was added to the 12 mL of ethanolic solution that contained 50 mg of Co-Fe PBA particles under stirring; the mixture was then transferred to a Teflon-lined stainless steel autoclave (25 mL) and kept at 120 °C for 6 h. The Co_3S_4 sample was finally obtained by the same process of centrifugation, drying, and annealing. MoS_2 nanosheets were prepared by mixing 20 mL of thioacetamide (0.1875 mM, ethanol) with 20 mL of $Na_2MoO_4 \cdot 2H_2O$ (0.0625 mM, water) under stirring for 30 min; the mixture solution was then transferred to an autoclave (50 mL) and kept at 200 °C for 12 h. After cooling to room temperature, the precipitates were washed with DI water and ethanol and dried at 60 °C overnight. Finally, the dried powder was heated at 350 °C for 2 h under a N_2 atmosphere to obtain MoS_2.

Physicochemical characterizations

Scanning electron microscopy (SEM) images were obtained on a Hitachi SU-8000 instrument at high vacuum with an acceleration voltage of 5 kV. X-ray diffraction (XRD) patterns were performed on a Rigaku RINT 2000X-ray diffractometer at 40 kV and 40 mA with monochromatic Cu Kα radiation at a scanning rate of 1 °C·min^{-1}. The transmission electron microscopy (TEM) and elemental mapping analysis were carried out to investigate the inner structures of the samples using a JEM-2100F operated at 200 kV. X-ray photoelectron spectroscopy (XPS) spectra were acquired by using a PHI Quantera SXM (ULVAC-PHI) instrument with an Al Kα X-ray source. All binding energies were calibrated via referencing to C 1 s binding energy (285.0 eV).

Electrochemical measurements

Typically, 2 mg of catalyst was dispersed into a mixed solvent containing 25 μL of Nafion solution (5 wt%) and 475 μL of ethanol/water (volume ratio is 1:3) to form a homogeneous ink with the assistance of sonication. Then, 5 μL of the ink was dropped onto the surface of the polished glassy carbon electrode (GCE, 3 mm diameter) and

dried naturally at room temperature. The mass loading of active materials is 0.283 $mg \cdot cm^{-2}$. All electrochemical measurements were performed using a CHI 660EZ electrochemical workstation with a conventional three-electrode cell. The modified GCE, a graphite rod and a saturated calomel electrode (SCE, 0.241V *vs.* RHE) served as a working electrode, a counter electrode and a reference electrode, respectively. Polarization curves for both OER and HER activities were characterized by linear sweep voltammetry (LSV) with a scan rate of 5 $mV \cdot s^{-1}$. All plots displayed were calibrated to a reversible hydrogen electrode (RHE) based on the equation ($E_{RHE} = E_{SCE} + 0.059 \times pH + 0.241$) and corrected against the iR compensation. The overpotential (η) for the OER was calculated according to the following formula: $\eta(V) = E_{RHE} - 1.23$ V. Electrochemical impedance spectroscopy (EIS) was obtained by applying an AC voltage with a 10 mV amplitude in a frequency range from 1 to 100000 Hz and recorded at -0.1 V *vs.* RHE for the HER and 1.3 V *vs.* RHE for the OER in 1 M KOH. The electrical double-layer specific capacitors (C_{dl}) of the materials were measured by conducting cyclic voltammetry (CV) at non-Faradaic overpotentials ranging from 1.3 to 1.4 V (*vs.* RHE, in 1 M KOH) with sweep rates of 10, 20, 40, 60, and 80 mV s^{-1}. The plot current density between the anodic and cathodic sweeps against the scan rate had a liner relationship, and its slope was equivalent to twice the double-layer capacitance (C_{dl}).

Preparation of a Co_3S_4@MoS_2 two-electrode setup

Typically, a 5 mg sample of Co_3S_4@MoS_2 was dispersed in a water/ethanol solution (500 μL, 3:1 v/v) with 25 μL of Nafion solution by sonicating for 1 h to form a homogeneous ink. Then, 15 μL of the uniform ink was dropped onto carbon fiber paper (0.5×0.5 cm^2) and dried at room temperature (mass loading: 0.6 $mg \cdot cm^{-2}$). Carbon fiber paper was chosen as the conductive substrate because it is porous and has negligible catalytic or noncatalytic activity in the surveyed potential region in this work.

3. Results and discussion

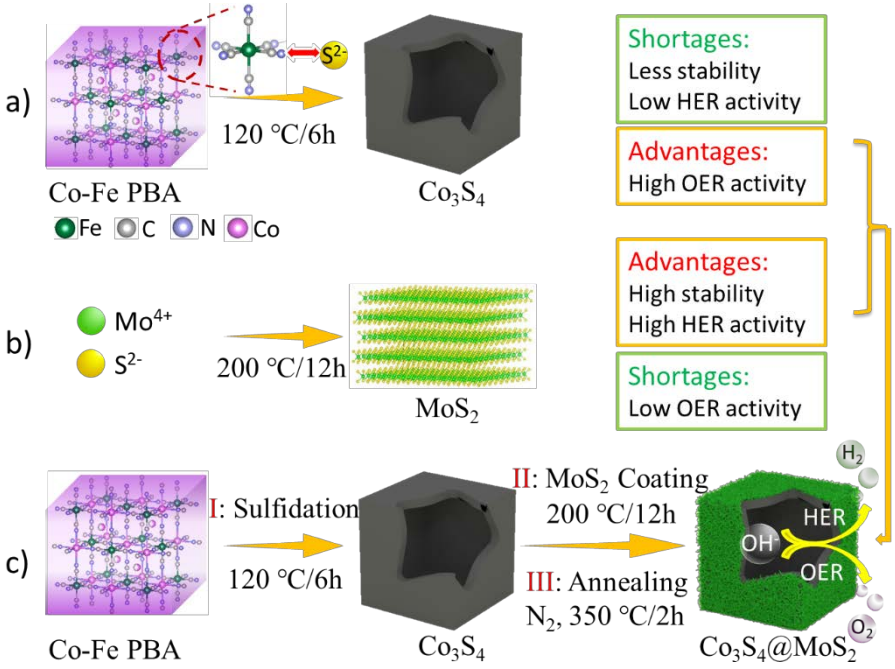

Fig. 1. Schematic illustration for the preparation of a) hollow Co_3S_4 nanoboxes via one-step solvothermal sulfidation reaction at 120 °C, b) MoS_2 nanosheets via one-step solvothermal reaction at 200 °C, and c) hollow Co_3S_4@MoS_2 heterostructure via two-step temperature-raising hydrothermal procedure (I: Sulfidation, II: *in situ* MoS_2 coating on the surface of Co_3S_4) and subsequent thermal annealing process under a N_2 atmosphere (III).

The procedures for fabricating Co_3S_4@MoS_2 are illustrated in **Fig. 1.** Crystalline Co-Fe PBA with a well-defined nanocubic structure was first prepared. Scanning electron microscopy (SEM) images in **Fig. S1a** show that the obtained Co-Fe PBA nanocubes have a uniform distribution with an average size of ~200 nm. The X-ray diffraction (XRD) pattern in **Fig. S1b** reveals that all peaks of the as-synthesized sample are well matched with typical Co-Fe PBA, which is basically consistent with the previous work [20]. As shown in **Fig. 1a** and **Fig. 1c**, hollow Co_3S_4 nanoboxes were formed through ionic exchange reaction between $Fe(CN)_6^{3-}$ in Co-Fe PBA and S^{2-} when the hydrothermal temperature reaches 120 °C [20]; then layered MoS_2 grew onto the surfaces of hollow Co_3S_4 nanoboxes at the further elevated temperature of 200 °C (**Fig. 1b** and **Fig. 1c**). As a result, a highly crystalline core-shell

Co_3S_4@MoS_2 heterostructure was obtained by subsequent calcination at 350 °C for 2 h under a N_2 atmosphere.

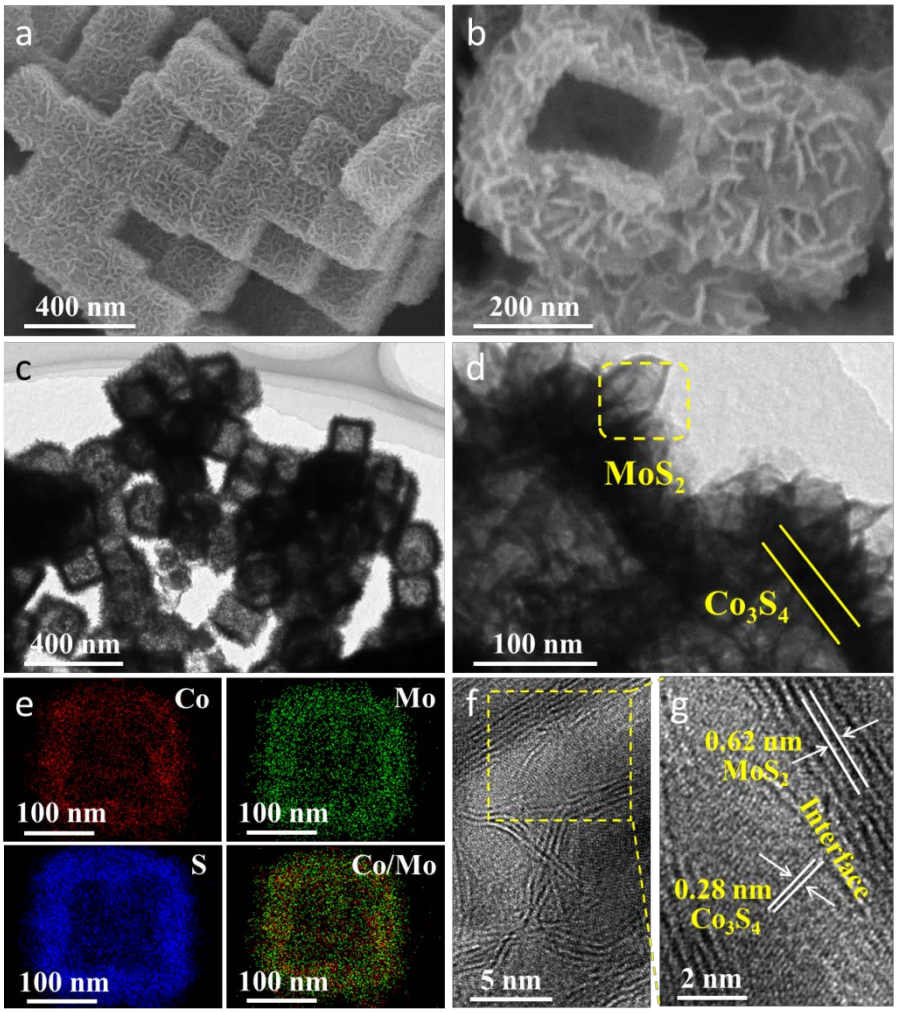

Fig. 2. (a, b) SEM images, (c, d) TEM images, (e) TEM-EDXS elemental mapping images, and (f, g) High resolution TEM images of hollow Co_3S_4@MoS_2 heterostructure.

Fig. 2**a** presents a scanning electron microscopy (SEM) image of the as-prepared sample, in which uniform cubic particles with rough surfaces can be observed, and the average size of the particles is ~250 nm. A closer SEM micrograph of a single cracked particle in Fig. 2**b** reveals a different hollow structure from the solid cubic Co-Fe PBA template, and the surfaces of the particles are decorated with random nanosheets. Transmission electron microscopy (TEM) images confirm that the particles are hollow structures that are constructed by dense inner Co_3S_4 nanoboxes and outer MoS_2 nanosheets to form core-shell structures (Fig. 2**c,d**). The elemental distribution

studied by STEM mappings is shown in Fig. 2**e,** revealing the distribution of Co, Mo, and S elements. When the signal areas of Co and Mo are overlapped, it is found that Co is surrounded by Mo, verifying the core-shell structure of Co_3S_4@MoS_2. Analysis of high-resolution TEM (HRTEM) images shows lattice fringes with spacings of 0.28 nm and 0.62 nm, which are indexed to the (311) plane of Co_3S_4 and the (002) plane of MoS_2, respectively. Furthermore, the image reveals the intimate contact of the Co_3S_4 and MoS_2, and the interfaces between these phases can be clearly identified (Fig. 2**f, g**).

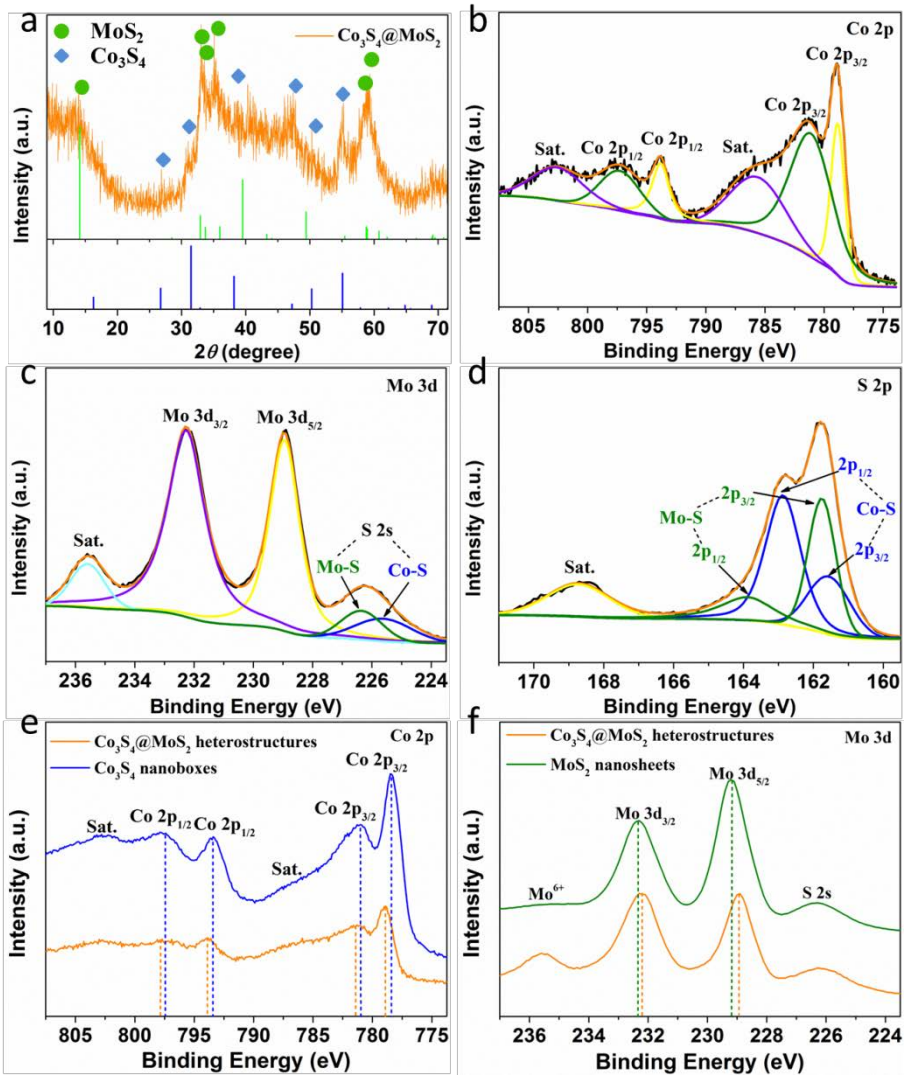

Fig. 3. (a) XRD pattern of synthesized Co_3S_4@MoS_2. The green and blue vertical lines indicate reference patterns of MoS_2 (JCPDS card no. 75-1539) and Co_3S_4 (JCPDS card no. 47-1738), respectively. (b–d) High-resolution XPS spectra of (b) Co

2p, (c) Mo 3d, and (d) S 2p of Co_3S_4@MoS_2. The contrast of (e) Co 2p spectra in Co_3S_4@MoS_2 and Co_3S_4, and (f) Mo 3d spectra in Co_3S_4@MoS_2 and MoS_2.

X-ray diffraction (XRD) patterns demonstrate the coexistence of Co_3S_4 and MoS_2 (**Fig. 3a**). The characteristic peaks located at 26.7°, 31.5°, 38.2°, 47.2°, 50.3°, and 55.1° correspond, respectively, to the (220), (311), (400), (422), (511), and (440) planes of Co_3S_4 (JCPDS no. 47-1738). The other peaks at 14.1°, 32.9°, 33.7°, 36.0°, 58.8°, and 58.9° are consistent, respectively, with the (002), (100), (101), (102), (110), and (008) planes of MoS_2 (JCPDS no. 75-1539). X-ray photoelectron spectroscopy (XPS) was carried out to investigate the chemical states of the Co_3S_4@MoS_2 heterostructure. The XPS survey spectrum indicates that the heterostructure consists of Mo, Co, S, and O (**Fig. S2**). The existence of oxide should be derived from the unavoidable surface oxidation of samples in the air. The high-resolution XPS spectrum of Co 2p in **Fig. 3b** can be deconvoluted into two spin-orbit doublets. The peaks at 778.8 eV and 793.8 eV are the first doublet (yellow lines), corresponding to Co $2p_{3/2}$ and Co $2p_{1/2}$, respectively. The second doublet is located at 781.2 eV (Co $2p_{3/2}$) and 797.3 eV (Co $2p_{1/2}$) (green lines). The other two broad peaks (violet lines) are related to shakeup satellites [31]. The Mo 3d spectrum in **Fig. 3c** reveals that there is a pair of peaks located at 228.9 eV and 232.2 eV, which are assigned to Mo $3d_{5/2}$ and Mo $3d_{3/2}$, respectively. The shoulder S 2s peak was deconvoluted into two peaks at 225.6 and 226.4 eV, indicative of the two chemical states of the S species bonding with Co and Mo ions, respectively. In the high-resolution S 2p spectrum (**Fig. 3d**), the peaks at 161.5 eV and 162.9 eV are pointed to the S $2p_{3/2}$ and S $2p_{1/2}$ of the Co-S bonds, respectively; the other two peaks at 161.8 eV and 163.9 eV are characteristic of the S $2p_{3/2}$ and S $2p_{1/2}$ of the Mo-S bonds, respectively, which is in good agreement with the previous report [32]. Notably, the binding energies of the Co $2p_{3/2}$ and Co $2p_{1/2}$ peaks in the Co_3S_4@MoS_2 heterostructures exhibit positive shifts of ~0.4 eV relative to that in the bare Co_3S_4, suggesting a strong interaction between the inner Co_3S_4 and the surrounding MoS_2 shell (**Fig. 3e**). Mo $3d_{5/2}$ and Mo $3d_{3/2}$ in Co_3S_4@MoS_2 negatively shift ~0.3 eV and ~0.1 eV, respectively, as compared to the

bare MoS_2 nanosheets, providing further evidence of the strong electronic interactions between the Co_3S_4 and MoS_2 (**Fig. 3f**) [23,24,33,34]. Therefore, the XPS results manifest the successful synthesis of Co_3S_4@MoS_2 core-shell architecture and also indicate the establishment of coupling interfaces.

In this work, an intellectual two-step temperature-raising hydrothermal reaction process was used to prepare the Co_3S_4@MoS_2 heterostructure. If the reaction was carried out directly at 200 °C for 12 h, the products show totally different morphologies. As shown in the SEM images (**Fig. S3**), the particles have two different morphologies. Some are formed by aggregated nanosheets (indicated by the green circle), others are cubic particles (indicated by the yellow square) without coating nanosheets (**Fig. S3b**). The formation of such an inhomogeneous product should be ascribed to the simultaneous sulfidation of Co-Fe PBA and formation of MoS_2 nanosheets during a one-step hydrothermal reaction process. To clarify the formation mechanism, the intermediate product was collected after the first reaction at 120 °C for 6 h and was characterized by SEM. **Fig. S4** illustrates that the intermediate product maintains the cubic frame and morphology of the Co-Fe PBA precursor, while the particles have rough surfaces that are composed of ultrafine nanoparticles. In addition, an interior void is visualized from a cracked nanoparticle (as indicated by the yellow circle). According to the above results, cobalt sulfide nanoboxes were probably firstly formed after 6 hours of hydrothermal reaction at 120 °C, and no MoS_2 nanosheets are formed at this stage. When the hydrothermal reaction temperature was increased to 200 °C, MoS_2 nanosheets started to grow on the surfaces of the cobalt sulfide nanoboxes. Finally, a well-dispersed hollow core-shell Co_3S_4@MoS_2 heterostructure was obtained.

Normally, the OER is regarded as the bottle-neck in many energy-related devices due to the sluggish multistep proton-coupled electron transfer processes [34]. The electrocatalytic properties of Co_3S_4@MoS_2 heterostructures for the OER were first evaluated by using a typical three-electrode system in a 1 M KOH aqueous electrolyte. To reveal the synergistic catalytic effect of Co_3S_4@MoS_2 heterostructures, bare Co_3S_4 and MoS_2 were also prepared and tested under identical conditions for

comparison (Fig. S5). Additionally, the recognized OER catalyst of RuO_2 was also measured as a benchmark. The linear sweep voltammetry (LSV) curves after iR compensation are displayed in Fig. 4**a**. Remarkably, the Co_3S_4@MoS_2 heterostructure exhibits better activity than do those of bare MoS_2 and Co_3S_4, with an overpotential of 280 mV at the current density of 10 mA·cm^{-2} (η_{10}), as compared with 300 mV for Co_3S_4 and 460 mV for MoS_2, highlighting the cooperative interactions between the Co_3S_4 and MoS_2. Noticeably, Co_3S_4@MoS_2 shows comparable activity to RuO_2 with the same overpotential of 280 mV at the current density of 10 mA·cm^{-2}. The Tafel slopes derived from the LSV curves (Fig. 4**b)** illustrate that Co_3S_4@MoS_2 heterostructure has the fastest kinetics for oxygen generation, with a corresponding Tafel slope of 43 mV·decade^{-1}, which is much smaller than the Co_3S_4 (61 mV·decade^{-1}) and even the RuO_2 (70 mV·decade^{-1}) catalysts. Impressively, the distinguished OER catalytic activity of Co_3S_4@MoS_2 outperforms most of the transition metal-based catalysts reported to date (Table S1).

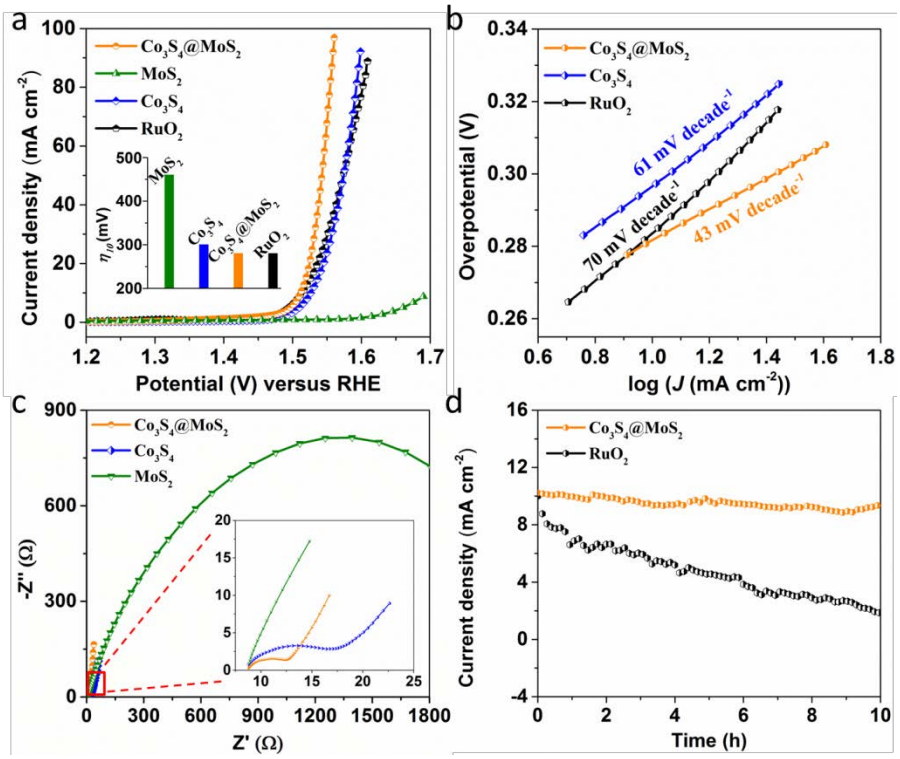

Fig. 4. (a) Polarization curves and (b) the corresponding Tafel plots of Co_3S_4@MoS_2, MoS_2, Co_3S_4, and RuO_2 electrodes for the OER in a 1 M KOH solution. (c) EIS Nyquist plot of different electrodes recorded at the same applied voltage (1.3 V *vs.*

RHE). (d) Chronoamperometric responses (*i*–*t*) collected on the Co_3S_4@MoS_2 electrode and commercial RuO_2 at the same applied potential of 1.51 V *vs.* RHE over 10 h in 1 M KOH. The insets in (a) are the OER overpotentials of catalysts at a current density of 10 $mA \cdot cm^{-2}$. The inset in (c) is the magnification of EIS Nyquist plots. All results shown are corrected by iR compensation. LSV scan rate: 5 $mV \cdot s^{-1}$.

Electrochemical impedance spectroscopy (EIS) measurements were conducted to explore the OER kinetics in catalysis at the same applied voltage (1.3 V *vs.* RHE). The Nyquist plots in **Fig. 4c** reveal that the Co_3S_4@MoS_2 heterostructure has smaller diameters of the semicircle registered at high frequencies as compared with pure Co_3S_4 and MoS_2, indicating lower charge-transfer resistance at the interface between the catalyst and electrolyte [35]. Usually, it is accepted that charge-transfer resistance is well correlated with electrocatalytic kinetics. XPS results (**Fig. 3e,f)** suggest that there is a strong electronic interaction between the inner Co_3S_4 core and the outer MoS_2 shell, thus nanointerfaces are probably formed between Co_3S_4 and MoS_2 in the Co_3S_4@MoS_2 heterostructures, affording good donor-acceptor electronic interaction between Co_3S_4 and MoS_2. This, in turn, greatly optimizes the electronic properties of the Co_3S_4@MoS_2, leading to an increased electrical conductivity and a higher catalytic kinetic of Co_3S_4@MoS_2 [36]. The unique synergistic effect between cobalt sulfide and molybdenum disulfide has been proposed by other works. Ramos et al. [37] built a model for a Co_9S_8/MoS_2 interface based on DFT and showed the creation of open latent vacancy sites on Mo atoms interacting with Co and the formation of Co-Mo bonds. Then a strong electron donation from Co to Mo also occurred through the intermediate sulfur atom's bonding to both metals. Thus, the charge-transfer resistance of the Co_9S_8/MoS_2 heterostructure was decreased. This proposition was further confirmed by Zhu and co-workers [33]. In their as-prepared Co_9S_8@MoS_2 core-shell system, the heterostructure showed lower charge-transfer resistance than did bare Co_9S_8 and MoS_2, which is beneficial for improved catalytic activity.

In addition, to gain insight into the effect of a cooperative system on Co_3S_4@MoS_2, cyclic voltammetry (CV) measurement was employed to acquire the

electrochemical double-layer capacitance (C_{dl}), which is assumed to be linearly proportionate to the electrochemical active surface area (ECSA). As shown in **Fig. S6**, CV curves at different scan rates (10, 20, 40, 60, and 80 $mV \cdot s^{-1}$) in a non-Faradaic region were collected for Co_3S_4, MoS_2, and $Co_3S_4@MoS_2$. By plotting the difference in current density between the anodic and cathodic sweeps at a given potential (1.36 V *vs.* RHE) against the scan rate, a linear curve was acquired. **Fig. S7** shows that the calculated C_{dl} of $Co_3S_4@MoS_2$ is 62 $mF \cdot cm^{-2}$, which is higher than that of Co_3S_4 (57 $mF \cdot cm^{-2}$) and MoS_2 (12 $mF \cdot cm^{-2}$). These results suggest that the fabricated $Co_3S_4@MoS_2$ heterostructure offers more active sites due to the constructed interfaces between Co_3S_4 and MoS_2, which should contribute to the enhanced OER electrocatalytic properties of $Co_3S_4@MoS_2$ [38]. As in agreement with previous report, new water splitting active sites could be formed due to the interfaces built in the fabricated MoS_2/Ni_3S_2 heterostructures, which are endowed with the enhanced electrocatalytic properties [23].

Stability and durability are also important criteria for evaluating the performance of electrocatalysts. The chronoamperometric responses (*i*–*t*) were first carried out on the $Co_3S_4@MoS_2$ electrode at the applied potential of 1.51 V (*vs.* RHE). **Fig. 4d** illustrates that the $Co_3S_4@MoS_2$ heterostructure shows negligible current density decay as compared with that of RuO_2 for more than 10 h, indicating the robust durability of $Co_3S_4@MoS_2$. In addition, continuous CV measurement at a potential range between 1.0 and 1.6 V (*vs.* RHE) with a scan rate of 100 $mV \cdot s^{-1}$ for 2000 cycles was also conducted to test the catalytic stability of the $Co_3S_4@MoS_2$ catalyst. As shown in **Fig. S8**, $Co_3S_4@MoS_2$ displays excellent stability without OER activity degradation, even after 2000 cycles of continuous CV measurement. The SEM image of $Co_3S_4@MoS_2$ (inset in **Fig. S8**) collected after the CV test shows that $Co_3S_4@MoS_2$ almost maintains its origin morphology, even after a long-term stability test. The excellent stability of $Co_3S_4@MoS_2$ should be attributed to the following factors: (i) The interfacial interaction between Co_3S_4 and MoS_2 enhances the density of electron transfer at the specific domains; (ii) a unique core-shell system is built by the highly active Co_3S_4 core, along with a more stable MoS_2 shell; (iii) the

hollow structure enables the easy release of bubbles formed on the surface of the electrode during operation, thus preventing the catalyst from being removed from the electrode.

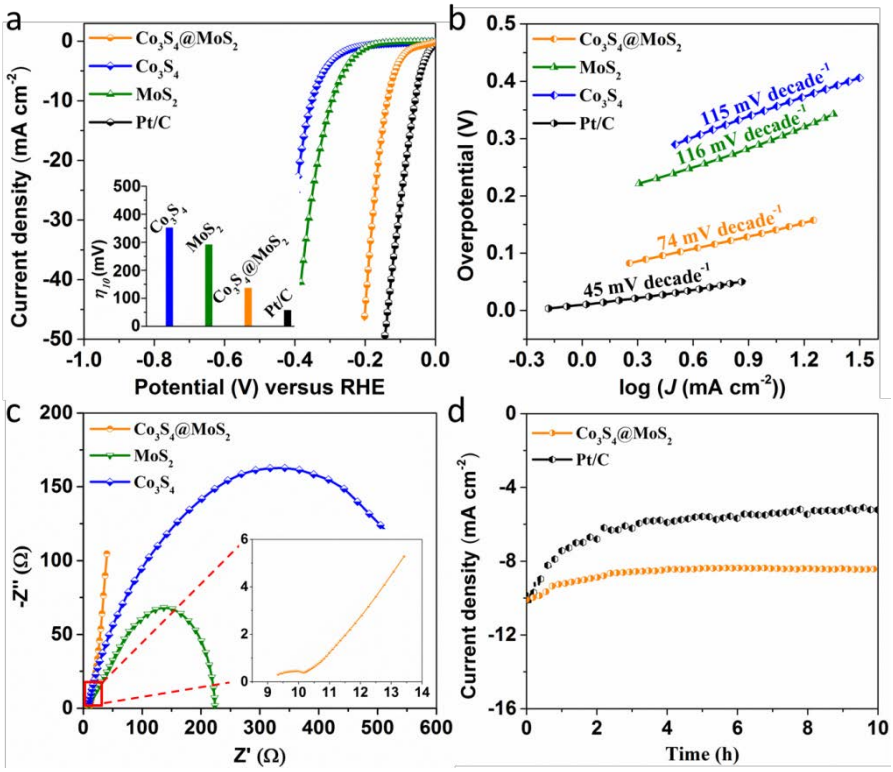

Fig. 5. (a) Polarization curves and (b) the corresponding Tafel plots of Co_3S_4@MoS_2, MoS_2, Co_3S_4, and Pt/C electrodes for the HER in a 1 M KOH solution. (c) The EIS Nyquist plot of different electrodes recorded at the same applied voltage (-0.1 V *vs.* RHE). (d) Chronoamperometric responses (*i*–*t*) collected on the Co_3S_4@MoS_2 electrode and commercial Pt/C at the applied potential of -136 mV and -57 mV (*vs.* RHE) over 10 h in 1 M KOH, respectively. The inset in (a) shows the HER overpotentials of catalysts at a current density of 10 mA·cm^{-2}. The inset in (c) shows the magnification of the EIS Nyquist plot.

Likewise, the electrocatalytic HER performance of as-prepared samples in alkaline environment was also evaluated. For comparison, the commercially available 20 wt% Pt/C catalyst was measured. Fig. 5**a** displays the polarization curves after iR correction of Co_3S_4@MoS_2, Co_3S_4, MoS_2, and Pt/C with a scan rate of 5 mV·s^{-1} in 1.0 M KOH. Obviously, the Pt/C catalyst exhibits the best HER activity with an

overpotential of 57 mV at a current density of 10 mA·cm^{-2}. Although the HER activity of Co_3S_4@MoS_2 is inferior to that of the Pt/C electrode, it still demonstrates the structural advantages with a lower overpotential (η_{10} = 136 mV) as compared with that of bare MoS_2 (η_{10} = 291 mV) and Co_3S_4 (η_{10} = 351 mV). Furthermore, the corresponding Tafel slopes (**Fig. 5b**) are calculated to be 45, 74, 116, and 115 mV·decade^{-1} for Pt/C, Co_3S_4@MoS_2, MoS_2, and Co_3S_4, respectively, which suggests that the Co_3S_4@MoS_2 heterostructure can act as an ideal non-noble metal catalyst for hydrogen production. Generally, the HER in a basic environment has sluggish kinetics as compared to those in an acidic environment. The outstanding performance of Co_3S_4@MoS_2 for the HER in an alkaline environment is comparable to or even better than the as-reported catalysts to date (**Table S2**). EIS tests were also conducted to investigate electrode kinetics occurring at the electrode/electrolyte interface. As shown in **Fig. 5c**, the Nyquist plots indicate that Co_3S_4@MoS_2 has a lower charge transfer resistance than bare Co_3S_4 and MoS_2, indicating the rapid charge transfer that favors HER catalytic activity. In addition, both the long-term potential cycling test and time-dependent current density curves reveal that Co_3S_4@MoS_2 has excellent durability for the HER in alkaline media. The chronoamperometric curve of Co_3S_4@MoS_2 in **Fig. 5d** presents no appreciable decrease in current density over 10 h for hydrogen evolution as compared with the Pt/C electrode. Meanwhile, Co_3S_4@MoS_2 shows a very slight decrease of HER activity after continuous 2000 CV cycles (**Fig. S9**), and the morphology also keeps the original structure after a long-term stability test (inset in **Fig. S9**).

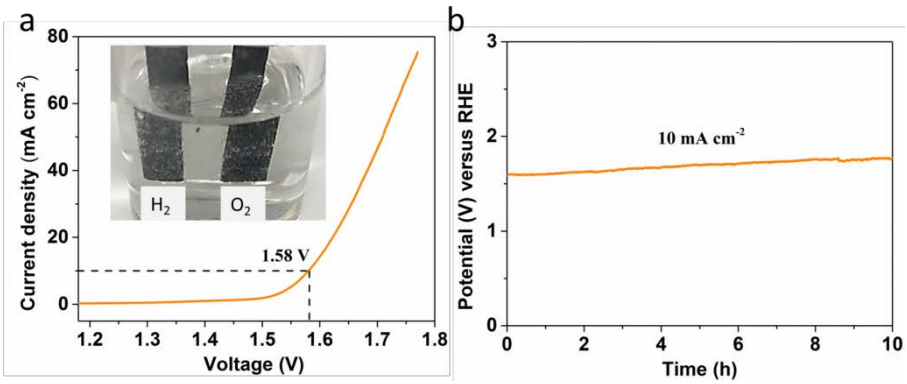

Fig. 6. (a) Polarization curves of the overall water splitting using Co_3S_4@MoS_2 as

both anode and cathode at a scan rate of 5 $mV \cdot s^{-1}$ in 1 M KOH solution. (b) Chronopotentiometric curve of the $Co_3S_4@MoS_2$ electrode under a current density of 10 $mA \cdot cm^{-2}$.

All of the above results indicate that the $Co_3S_4@MoS_2$ heterostructure is an active and stable bifunctional electrocatalyst for both the HER and OER in an alkaline solution. Therefore, a two-electrode setup using $Co_3S_4@MoS_2$ as both the anode and cathode was assembled to investigate its catalytic activity for overall water splitting in a 1 M KOH solution. As shown in **Fig. 6a**, the $Co_3S_4@MoS_2$ electrode exhibits high activity, reaching a water-splitting current density of 10 $mA \cdot cm^{-2}$ at a voltage of 1.58 V, which compares favorably to other recently reported nonprecious overall water splitting electrocatalysts, such as Ni@NC-800 (ca. 1.60 V) [39], MoO_2/Ni (ca. 1.73 V) [40], and Ni_3S_2/Ni foam (ca. 1.76 V) [41] (**Fig. S10**). The inset in **Fig. 6a** shows that abundant H_2 and O_2 were produced from the respective $Co_3S_4@MoS_2$ electrode. Additionally, the chronopotentiometric curve in **Fig. 6b** reveals that $Co_3S_4@MoS_2$ is stable for at least 10 h. Such prominent activity demonstrates the potential application of $Co_3S_4@MoS_2$ for overall water splitting.

4. Conclusion

In summary, we developed a core-shell $Co_3S_4@MoS_2$ heterostructure by the *in situ* growth of MoS_2 nanosheets on the surfaces of hollow Co_3S_4 nanoboxes by carrying out a two-step temperature-raising hydrothermal reaction and thermal annealing processes. The elaborate combination of the more stable HER catalyst of MoS_2 with the remarkable OER catalyst of Co_3S_4 realizes a bifunctional catalyst. More importantly, the unique hollow and core-shell structure, and the synergistic effects of lower charge transfer resistances and abundant active sites formed by the Co_3S_4 and MoS_2 counterparts that endow the $Co_3S_4@MoS_2$ with outstanding electrocatalytic activity and good long-term stability. The strategy developed here provides new insight into the design of novel non-noble metal bifunctional catalysts as promising alternatives for overall water splitting.

Notes

The authors declare that they have no competing financial interests.

Acknowledgments

J.T. is an overseas researcher under Postdoctoral Fellowship of the Japan Society for the Promotion of Science (JSPS project number 17F17080).

Reference

[1] D. Larcher, J.-M. Tarascon, Nat. Chem. 7 **(**2015) 19–29.

[2] X. Chen, C. Li, M. Gra¨tzel, R. Kostecki, S. S. Mao, Chem. Soc. Rev. 41 (2012) 7909–7937.

[3] S. Chu, A. Majumdar, Nature 488 (2012) 294–303.

[4] Y. Jiao, Y. Zheng, M. Jaroniec, S. Z. Qiao, Chem. Soc. Rev. 44 (2015) 2060–2086.

[5] J. Wang, W. Cui, Q. Liu, Z. Xing, A. M. Asiri, X. Sun, Adv. Mater. 28 (2016) 215–230.

[6] C. G. Morales-Guio, L.-A. Stern, X. Hu, Chem. Soc. Rev. 43 (2014) 6555–6569.

[7] N.-T. Suen, S.-F. Hung, Q. Quan, N. Zhang, Y.-J. Xu, H. M. Chen, Chem. Soc. Rev. 46 (2017) 337–365.

[8] J. Li, G. Zheng, Adv. Sci. 4 (2017) 1600380.

[9] N. K. Chaudhari, H. Jin, B. Kim, K. Lee, Nanoscale 9 (2017) 12231–12247.

[10] Y. Zhang, Q. Zhou, J. Zhu, Q. Yan, S. X. Dou, W. Sun, Adv. Funct. Mater. 27 (2017) 1702317.

[11] Y. Yin, J. Han, Y. Zhang, X. Zhang, P. Xu, Q. Yuan, L. Samad, X. Wang, Y. Wang, Z. Zhang, P. Zhang, X. Cao, B. Song, S. Jin, J. Am. Chem. Soc. 138 (2016) 7965–7972.

[12] T. R. Hellstern, J. Kibsgaard, C. Tsai, D. W. Palm, L. A. King, F. Abild-Pedersen, T. F. Jaramillo, ACS Catal. 7 (2017) 7126−7130.

[13] Z. Shi, K. Nie, Z.-J. Shao, B. Gao, H. Lin, H. Zhang, B. Liu, Y. Wang, Y. Zhang, X. Sun, X.-M. Cao, P. Hu, Q. Gao, Y. Tang, Energy Environ. Sci. 10 (2017)

1262−1271.

[14] J.-S. Li, Y. Wang, C.-H. Liu, S.-L. Li, Y.-G. Wang, L.-Z. Dong, Z.-H. Dai, Y.-F. Li, Y.-Q. Lan, Nat. Commun. 7 (2016) 11204.

[15] Y. Shi, B. Zhang, Chem. Soc. Rev. 45 (2016) 1529−1541.

[16] X.-F. Lu, L.-F. Gu, J.-W. Wang, J.-X. Wu, P.-Q. Liao, G.-R. Li, Adv. Mater. 29 (2017) 1604437.

[17] L. Zhuang, L. Ge, Y. Yang, M. Li, Y. Jia, X. Yao, Z. Zhu, Adv. Mater. 29 (2017) 1606793.

[18] C. Andronescu, S. Barwe, E. Ventosa, J. Masa, E. Vasile, B. Konkena, S. Moller, W. Schuhmann, Angew. Chem. Int. Ed. 56 (2017) 11258–11262.

[19] X. Zou, Y. Liu, G.-D. Li, Y. Wu, D.-P. Liu, W. Li, H.-W. Li, D. Wang, Y. Zhang, X. Zou, Adv. Mater. 29 (2017) 1700404.

[20] P. Cai, J. Huang, J. Chen, Z. Wen, Angew. Chem. Int. Ed. 56 (2017) 4858–4861.

[21] Y. Liu, Q. Li, R. Si, G.-D. Li, W. Li, D.-P. Liu, D. Wang, L. Sun, Y. Zhang, X. Zou, Adv. Mater. 29 (2017) 1606200.

[22] J. Staszak-Jirkovský, C. D. Malliakas, P. P. Lopes, N. Danilovic, S. S. Kota, K.-C. Chang, B. Genorio, D. Strmcnik, V. R. Stamenkovic, M. G. Kanatzidis, N. M. Markovic, Nat. Mater. 15 (2016) 197–203.

[23] J. Zhang, T. Wang, D. Pohl, B. Rellinghaus, R. Dong, S. Liu, X. Zhuang, X. Feng, Angew. Chem. Int. Ed. 55 (2016) 6702–6707.

[24] Y. Hou, M. Qiu, G. Nam, M. G. Kim, T. Zhang, K. Liu, X. Zhuang, J. Cho, C. Yuan, X. Feng, Nano Lett. 17 (2017) 4202−4209.

[25] R. E. Morris, L. Brammer, Chem. Soc. Rev. 46 (2017) 5444−5462.

[26] Y.-B. Huang, J. Liang, X.-S. Wang, R. Cao, Chem. Soc. Rev. 46 (2017) 126−157.

[27] Y. V. Kaneti, J. Tang, R. R. Salunkhe, X. Jiang, A. Yu, K. C.-W. Wu, Y. Yamauchi, Adv. Mater. 29 (2017) 1604898.

[28] Z.-F. Huang, J. Song, K. Li, M. Tahir, Y.-T. Wang, L. Pan, L. Wang, X. Zhang, J.-J. Zou, J. Am. Chem. Soc. 138 (2016) 1359−1365.

[29] X.-Y. Yu, L. Yu, H. B. Wu, X. W. Lou, Angew. Chem. Int. Ed. 54 (2015) 5331–5335.

[30] C. Xing, Y. Liu, Y. Su, Y. Chen, S. Hao, X. Wu, X. Wang, H. Cao, B. Li, ACS Appl. Mater. Interfaces 8 (2016) 15430−15438.

[31] Y. Guo, J. Tang, H. Qian, Z. Wang, Y. Yamauchi, Chem. Mater. 29 (2017) 5566−5573.

[32] X. Yang, H. Sun, P. Zan, L. Zhao, J. Lian, J. Mater. Chem. A 4 (2016) 18857–18867.

[33] H. Zhu, J. Zhang, R. Yanzhang, M. Du, Q. Wang, G. Gao, J. Wu, G. Wu, M. Zhang, B. Liu, J. Yao, X. Zhang, Adv. Mater. 27 (2015) 4752–4759.

[34] C. Du, M. Shang, J. Mao, W. Song, J. Mater. Chem. A 5 (2017) 15940–15949.

[35] M. Zheng, J. Du, B. Hou, C.-L. Xu, ACS Appl. Mater. Interfaces 9 (2017) 26066−26076.

[36] J. Bai, T. Meng, D. Guo, S. Wang, B. Mao, and M. Cao, ACS Appl. Mater. Interfaces 10 (2018) 1678-1689.

[37] M. Ramos, G. Berhault, D. A. Ferrer, B. Torres, R. R. Chianelli, Catal. Sci. Technol. 2 (2012) 164–178.

[38] J. Kibsgaard, Z. Chen, B. N. Reinecke, T. F. Jaramillo, Nat. Mater. 11 (2012) 963–969.

[39] Y. Xu, W. Tu, B. Zhang, S. Yin, Y. Huang, M. Kraft, R. Xu, Adv. Mater. 29 (2017) 1605957.

[40] Y. Jin, H. Wang, J. Li, X. Yue, Y. Han, P. K. Shen, Y. Cui, Adv. Mater. 28 (2016) 3785–3790.

[41] L.-L. Feng, G. Yu, Y. Wu, G.-D. Li, H. Li, Y. Sun, T. Asefa, W. Chen, X. Zou, J. Am. Chem. Soc. 137 (2015) 14023−14026.

Table of Content

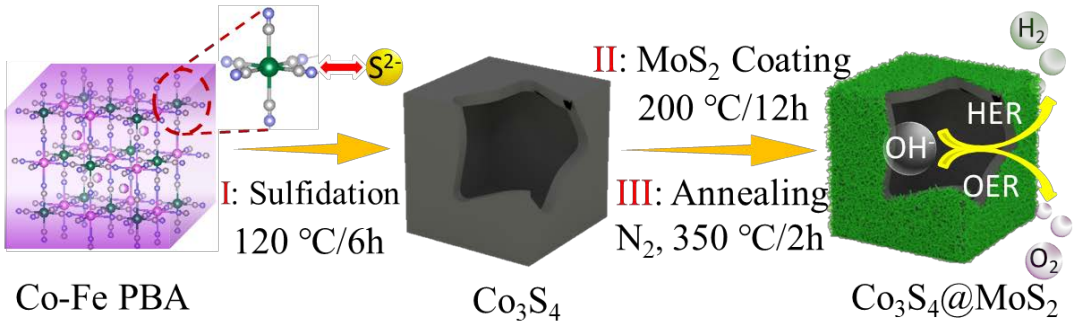

Supporting Information

Elaborately Assembled Transition Metal Chalcogels as a Bifunctional Catalyst for Highly Efficient Electrochemical Overall Water Splitting

Yanna Guo,[a,b] Jing Tang,[a]* Zhongli Wang,[a] Yoshio Bando,[a,c] and Yusuke Yamauchi[a,b,c,d]*

[a] International Center for Materials Nanoarchitectonics (MANA), National Institute for Materials Science (NIMS), 1-1 Namiki, Tsukuba, Ibaraki 305-0044, Japan. E-mail: TANG.Jing@nims.go.jp

[b] Faculty of Science and Engineering, Waseda University, 3-4-1 Okubo, Shinjuku, Tokyo 169-8555, Japan

[c] Australian Institute for Innovative Materials (AIIM), University of Wollongong, North Wollongong, NSW 2500, Australia. E-mail: yusuke@uow.edu.au

[d] School of Chemical Engineering and Australian Institute for Bioengineering and Nanotechnology (AIBN), The University of Queensland, Brisbane, QLD 4072, Australia

Fig. S1

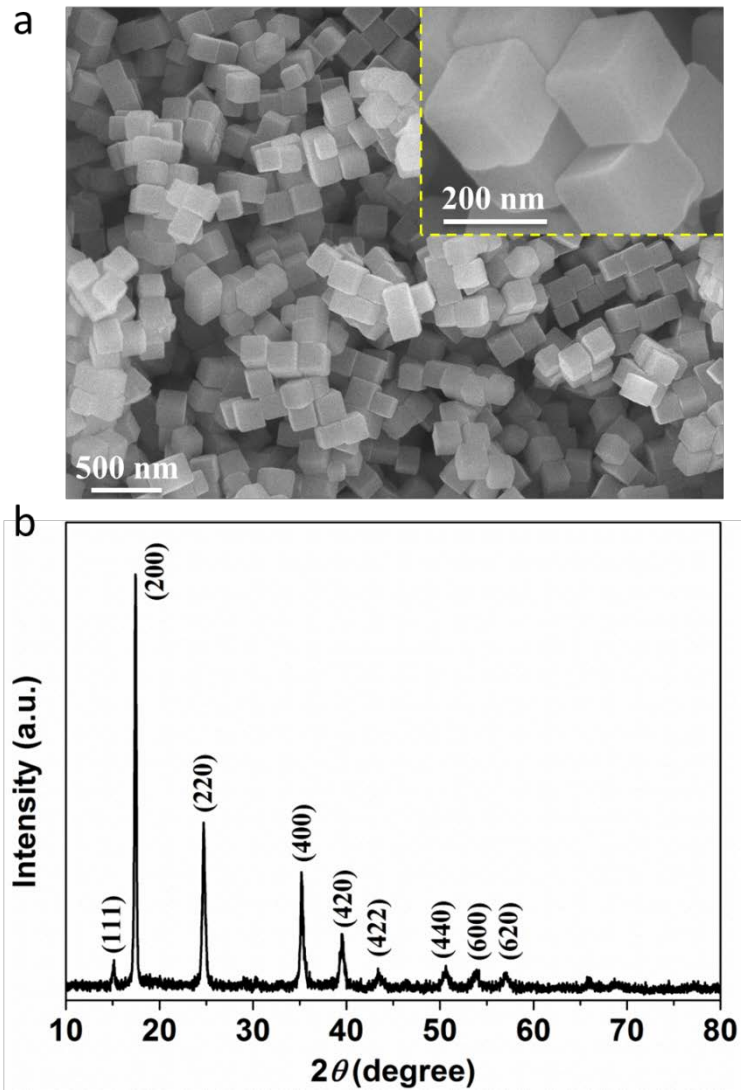

Fig. S1. (a) SEM images and (b) XRD pattern of a Co-Fe PBA precursor. The inset in (a) is a magnified SEM image of Co-Fe PBA particles.

Fig. S2

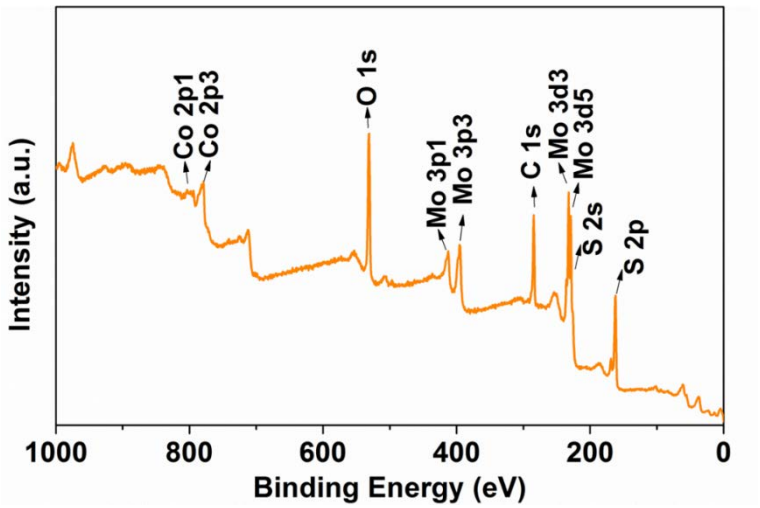

Fig. S2. XPS spectrum of the obtained Co_3S_4@MoS_2 heterostructure.

Fig. S3

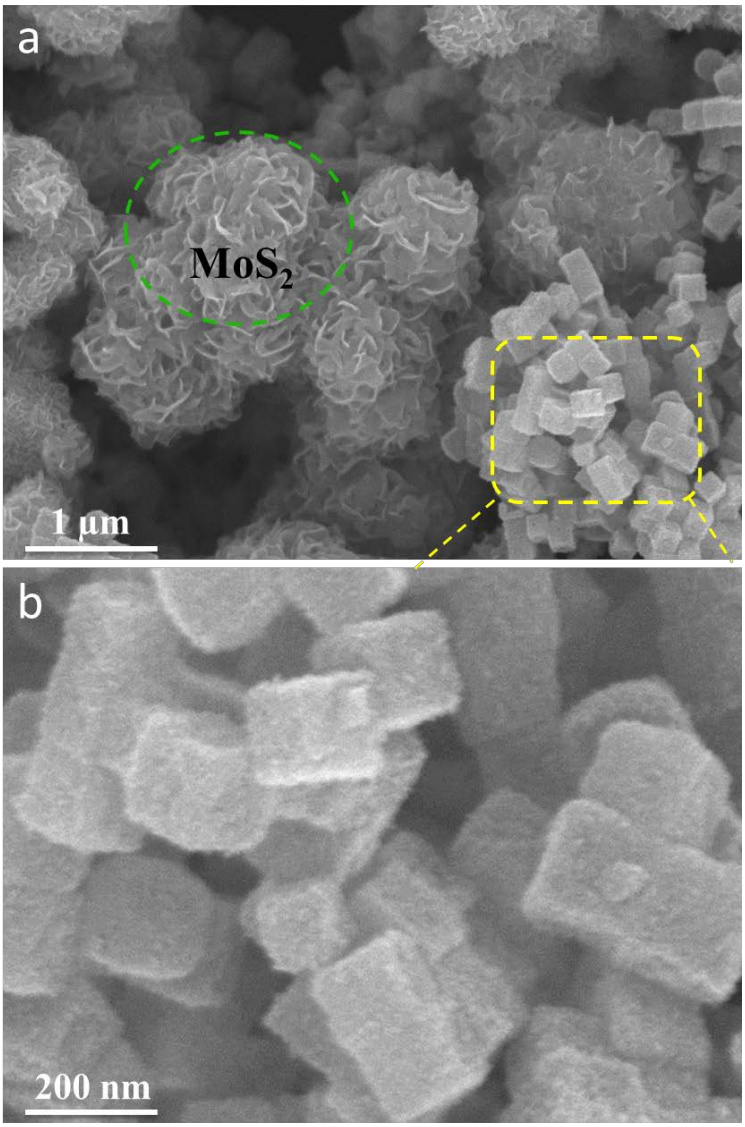

Fig. S3. (a) SEM image of the sample obtained by one-step temperature-raising hydrothermal reaction process by keeping the reaction at 200 °C for 12 h and (b) corresponding magnified SEM image of the selected area in (a).

Fig. S4

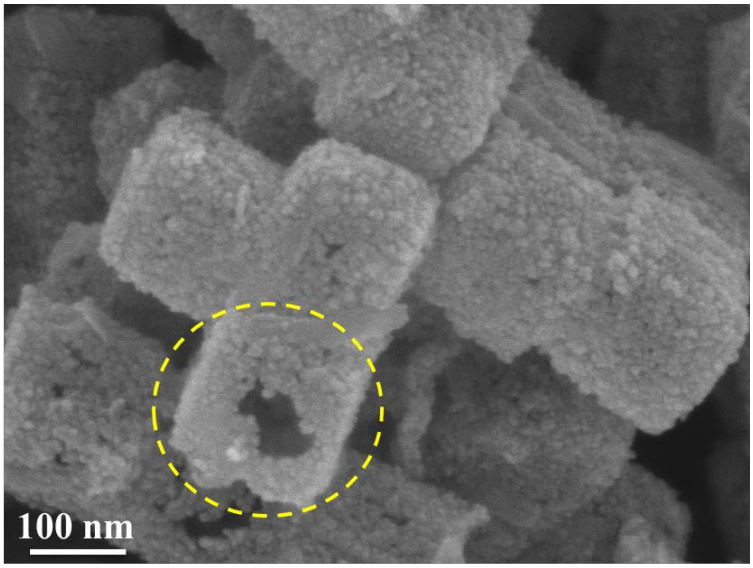

Fig. S4. SEM image of the intermediate product obtained after hydrothermal reaction at 120 °C for 6 h.

Fig. S5

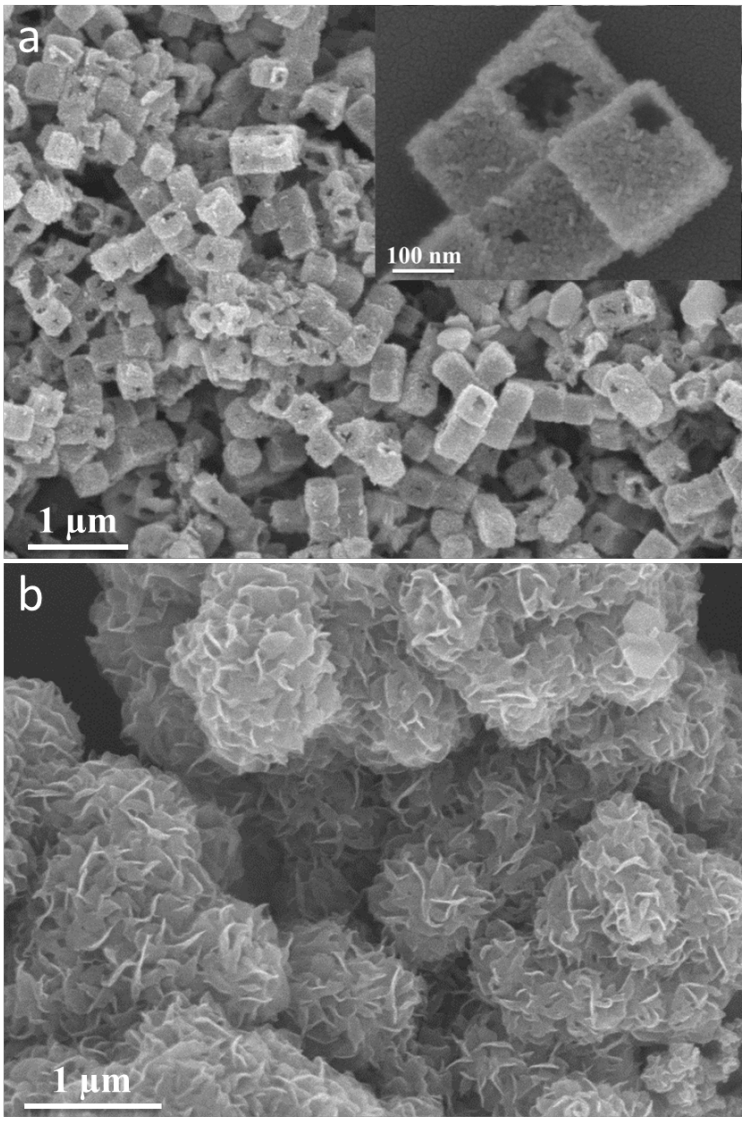

Fig. S5. SEM images of individual Co_3S_4 nanoboxes (a) and MoS_2 nanosheets (b). The inset in (a) is the magnified SEM image of Co_3S_4 particles.

Fig. S6

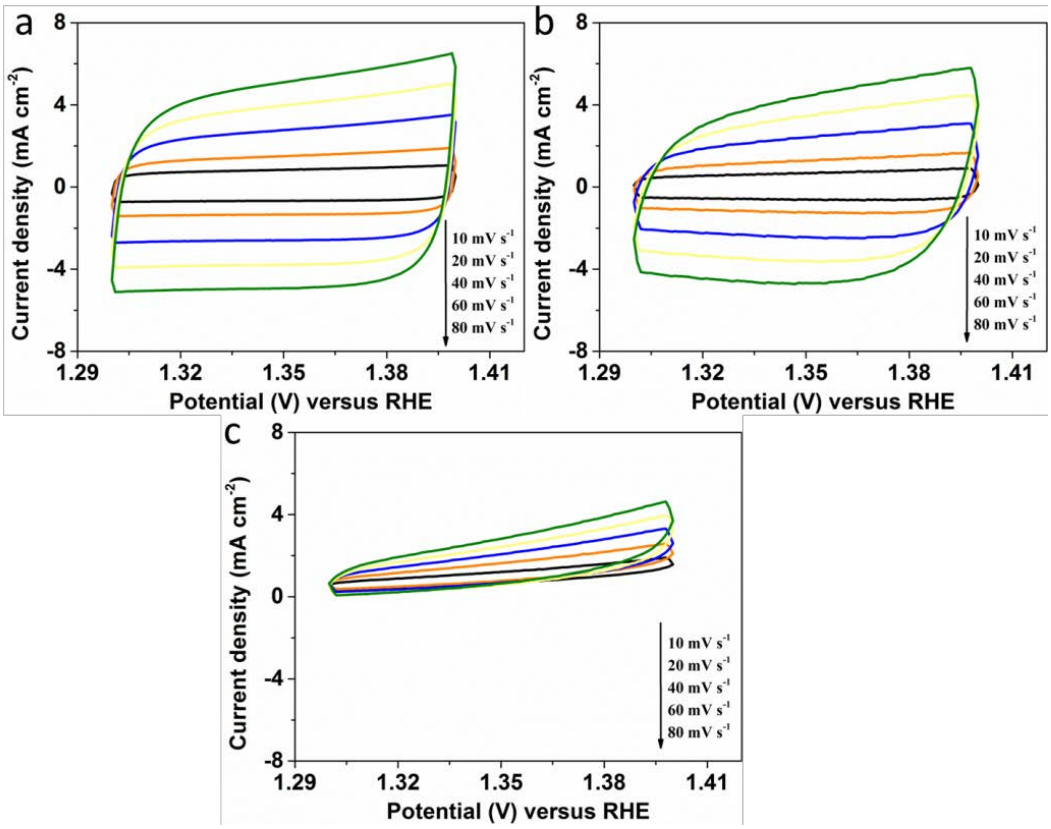

Fig. S6. Cyclic voltammograms of (a) Co_3S_4@MoS_2, (b) Co_3S_4, and (c) MoS_2 with various scan rates in a 1 M KOH solution.

Fig. S7

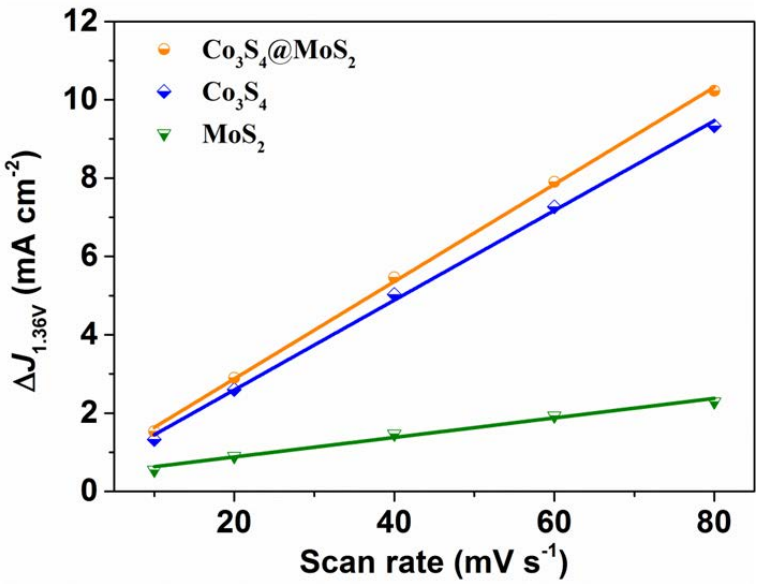

Fig. S7. Linear slopes were plotted from the cyclic voltammograms (**Figure S10**) of Co_3S_4@MoS_2, MoS_2, and Co_3S_4 in 1 M KOH. The linear slopes are equivalent to twice the double-layer capacitance (C_{dl}).

Fig. S8

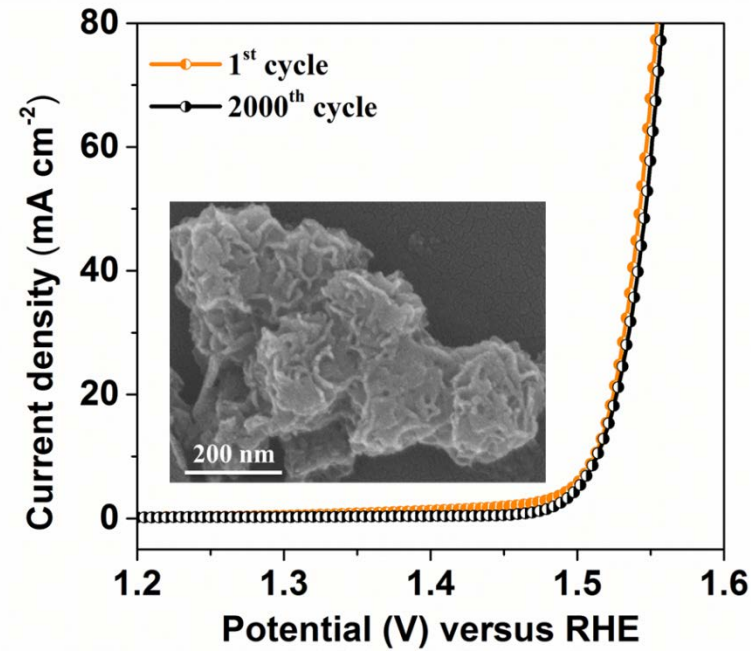

Fig. S8. LSV curves of Co_3S_4@MoS_2 obtained from the first and the 2000th cycles in 1 M KOH for the OER. The inset is the SEM image of Co_3S_4@MoS_2 after 2000 cycles of continuous CV measurements in 1 M KOH.

Fig. S9

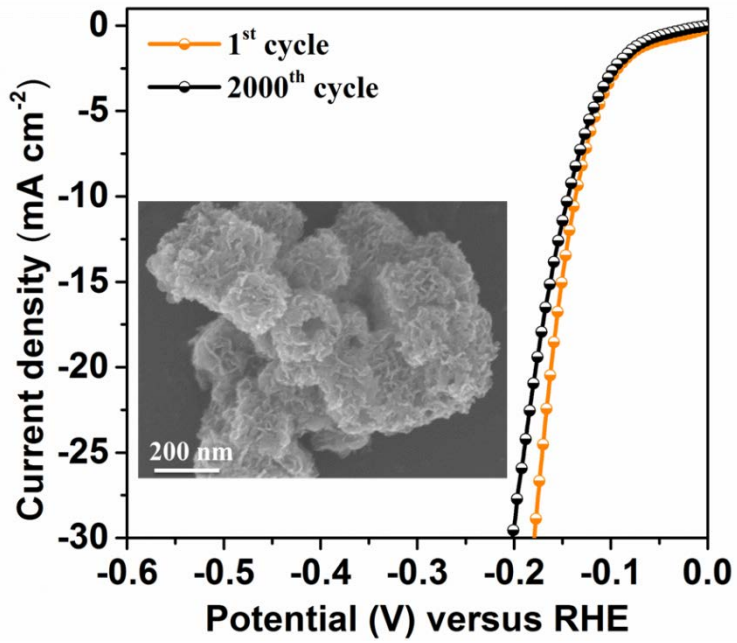

Fig. S9. LSV curves of Co_3S_4@MoS_2 obtained from the first and the 2000th cycles in 1 M KOH for the HER. The inset is the SEM image of Co_3S_4@MoS_2 after 2000 cycles of continuous CV measurements in 1 M KOH.

Fig. S10

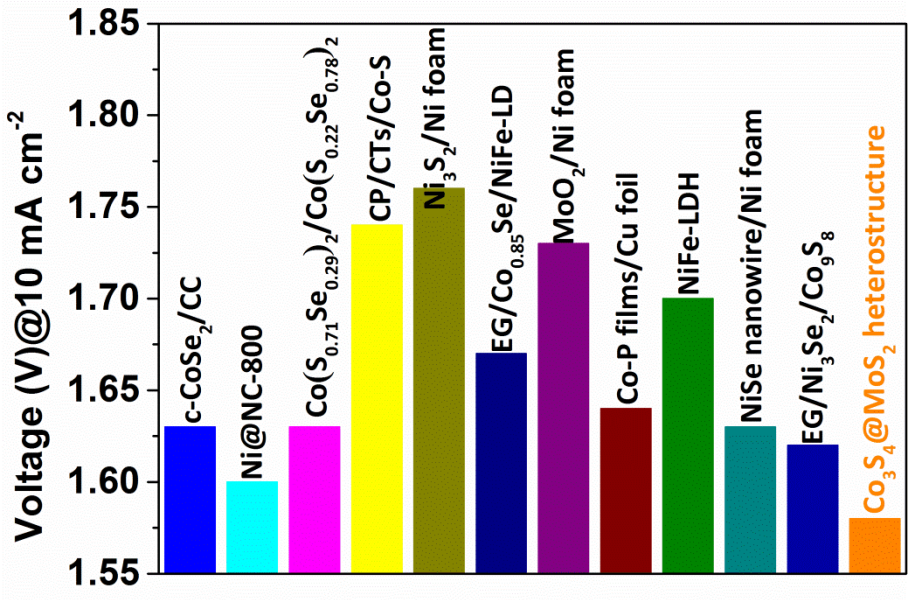

Fig. S10. Comparison of the electrochemical overall water splitting performance of the Co_3S_4@MoS_2 heterostructure with some representative reported non-precious bifunctional electrocatalysts at 10 mA·cm^{-2} in 1 M KOH.

Table S1. Comparison of the OER performance for Co_3S_4@MoS_2 with other electrocatalysts.

Catalysts	Current density (j, mA cm^{-2})	η at corresponding j (mV)	Tafel slope (mV·dec^{-1})	Electrolytes
Co_3S_4@MoS_2 (this work)	10	280	43	1 M KOH
Ni@NC-800[S1]	10	280	45	1 M KOH
$Co(S_{0.22}Se_{0.78})_2$[S2]	10	283	66	1 M KOH
Co_9S_8@MoS_2/CNFs[S3]	10	361	61	1 M KOH
MoS_2-Ni_3S_2 HNRs/NF[S4]	10	249	57	1 M KOH
Co_3O_4/$NiCo_2O_4$[S5]	10	340	88	1 M KOH
Co-P Film[S6]	10	345	47	1 M KOH
n-NiFe LDH/NGF[S7]	10	337	45	0.1 M KOH
NiCo LDHs[S8]	10	367	40	1 M KOH
Ultrathin Co_3S_4 nanosheet[S9]	10	355	48	0.1 M KOH
Co phosphide/phosphate[S10]	30	330	65	1 M KOH

Table S2. Comparison of the HER performance of Co_3S_4@MoS_2 with other electrocatalysts

Catalysts	Current density (j, mA cm^{-2})	η at corresponding j (mV)	Tafel slope (mV·dec^{-1})	Electrolytes
Co_3S_4@MoS_2 (this work)	10	136	74	1 M KOH
Ni@NC-800[S1]	10	205	160	1 M KOH
$Co(S_{0.71}Se_{0.29})_2$[S2]	10	122	86	1 M KOH
Co phosphide/phosphate[S10]	30	430	—	1 M KOH
NiFe LDHNS@DG10[S11]	10	300	110	1 M KOH
c-$CoSe_2$/CC[S12]	10	190	85	1 M KOH
$NiMo_3S_4$[S13]	10	252	98	0.1 M KOH
EG/Ni_3Se_2/Co_9S_8[S14]	20	170	83	1 M KOH
NF-Ni_3Se_2/Ni[S15]	10	203	79	1 M KOH
ONPPGC/ OCC[S16]	10	446	154	1 M KOH
$Ni_{1-x}Fe_x$/NC[S17]	10	230	111	1 M KOH
$NiCo_2S_4$@NiFe LDH/NF[S18]	10	200	101	1 M KOH
Co-NRCNTs[S19]	10	370	—	1 M KOH

[S1] Y. Xu, W. Tu, B. Zhang, S. Yin, Y. Huang, M. Kraft, R. Xu, Adv. Mater. 29 (2017) 1605957.

[S2] L. Fang, W. Li, Y. Guan, Y. Feng, H. Zhang, S. Wang, Y. Wang, Adv. Funct. Mater. 27 (2017) 1701008.

[S3] H. Zhu, J. Zhang, R. Yanzhang, M. Du, Q. Wang, G. Gao, J. Wu, G. Wu, M. Zhang, B. Liu, J. Yao, X. Zhang, Adv. Mater. 27 (2015) 4752–4759.

[S4] Y. Yang, K. Zhang, H. Lin, X. Li, H. C. Chan, L. Yang, Q. Gao, ACS Catal. 7 (2017) 2357–2366.

[S5] H. Hu, B. Guan, B. Xia, X. W. Lou, J. Am. Chem. Soc. 137 (2015) 5590–5595.

[S6] N. Jiang, B. You, M. Sheng, Y. Sun, Angew. Chem. Int. Ed. 54 (2015) 6251–6254.

[S7] C. Tang, H.-S. Wang, H.-F. Wang, Q. Zhang, G.-L. Tian, J.-Q. Nie, F. Wei, Adv. Mater. 27 (2015) 4516–4522.

[S8] F. Liang, F. Meng, M. Cabán-Acevedo, L. Li, A. Forticaux, L. Xiu, Z. Wang, S. Jin, Nano Lett. 15 (2015) 1421–1427.

[S9] Y. Liu, C. Xiao, M. Lyu, Y. Lin, W. Cai, P. Huang, W. Tong, Y. Zou, Y. Xie, Angew. Chem. Int. Ed. 54 (2015) 11231–11235.

[S10] Y. Yang, H. Fei, G. Ruan, J. M. Tour, Adv. Mater. 27 (2015) 3175–3180.

[S11] Y. Jia, L. Zhang, G. Gao, H. Chen, B. Wang, J. Zhou, M. T. Soo, M. Hong, X. Yan, G. Qian, J. Zou, A. Du, X. Yao, Adv. Mater. 29 (2017) 1700017.

[S12] P. Chen, K. Xu, S. Tao, T. Zhou, Y. Tong, H. Ding, L. Zhang, W. Chu, C. Wu, Y. Xie, Adv. Mater. 28 (2016) 7527–7532.

[S13] J. Jiang, M. Gao, W. Sheng, Y. Yan, Angew. Chem. Int. Ed. 55 (2016) 1–6.

[S14] Y. Hou, M. Qiu, G. Nam, M. G. Kim, T. Zhang, K. Liu, X. Zhuang, J. Cho, C. Yuan, X. Feng, Nano Lett. 17 (2017) 4202−4209.

[S15] R. Xu, R. Wu, Y. Shi, J. Zhang, B. Zhang, Nano Energy 24 (2016) 103−110.

[S16] J. Lai, S. Li, F. Wu, M. Saqib, R. Luque, G. Xu, Energy Environ. Sci. 9 (2016) 1210−1214.

[S17] X. Zhang, H. Xu, X. Li, Y. Li, T. Yang, Y. Liang, ACS Catal. 6 (2016) 580–588.

[S18] J. Liu, J. Wang, B. Zhang, Y. Ruan, L. Lv, X. Ji, K. Xu, L. Miao, J. Jiang, ACS

Appl. Mater. Interfaces 9 (2017) 15364−15372.

[S19] X. Zou, X. Huang, A. Goswami, R. Silva, B. R. Sathe, E. Mikmekova, T. Asefa, Angew. Chem. Int. Ed. 53 (2014) 4372–4376.